Oya *et al.*
Progress in Earth and Planetary Science 2022, **9**(1):18
https://doi.org/10.1186/s40645-022-00476-5

Progress in Earth and Planetary Science

RESEARCH ARTICLE

Open Access

Peridotites with back-arc basin affinity exposed at the southwestern tip of the Mariana forearc

Shoma Oya[1], Katsuyoshi Michibayashi[2,3*], Yasuhiko Ohara[2,3,4], Fernando Martinez[5], Fatma Kourim[6], Hao-Yang Lee[6] and Kohei Nimura[2]

Abstract

Peridotites at water depths of 3430 to 5999 m have been discovered using the submersible *Shinkai6500* (dives 6K-1397 and 6K-1398) on the southwestern slope of the 139°E Ridge (11°12′N, 139°15′E), a small ridge at the southwesternmost tip of the Mariana forearc near the junction with the Yap Trench and Parece Vela Basin. The peridotites studied consist of 17 residual harzburgites and one dunite and show various textures with respect to their depths. Peridotites with coarse-grained (> 1 mm) textures were sampled from the shallowest part (3705–4042 m) of the dive area, and peridotites with fine-grained (< 0.5 mm) textures were sampled deeper (5996 m). Olivine crystal-fabrics vary with grain size, with (010)[100] A-type patterns for the coarse-grained peridotites, {0kl}[100] D-type patterns for the fine-grained peridotites, and various indistinct patterns in samples of variable grain sizes. Fine-grained peridotites with D-type olivine crystal-fabrics could result from deformation under relatively higher flow stresses, suggesting that a ductile shear zone in the lithospheric mantle could occur in the deepest part of 139°E Ridge. Spinel Cr# range from relatively low (0.36) to moderately high (up to 0.57), and correlate with Ti contents (0.07–0.45 wt.%). The trace element patterns of clinopyroxene similarly exhibit steepening slopes from the middle to the light REEs regardless of textural variations. These mineralogical and geochemical features would result from melt-rock interactions under conditions of relatively shallow lithospheric mantle, which are much more comparable with the Parece Vela Basin peridotites than the Mariana forearc peridotites. Consequently, the Parece Vela Basin mantle is more likely exposed on the inner slope of the westernmost Mariana Trench, presumably due to the collision of the Caroline Ridge.

Keywords: Southern Mariana trench, Parece Vela basin, Peridotite, Olivine fabric, Mineral composition, Melt-rock interaction

1 Introduction

The southern Mariana forearc is a non-accretionary convergent plate margin, where the rock suites cropped out on the landside slope are similar to those found in many ophiolites (Bloomer and Hawkins 1983; Reagan et al. 2013; Stern et al. 2020). However, mantle peridotites in the southern Mariana forearc are only partly understood (Ohara and Ishii 1998; Michibayashi et al. 2009; Sato and Ishii 2011; Michibayashi et al. 2016a; Reagan et al. 2018). Previous geological expeditions to the eastern side of the Challenger Deep have found trench peridotites at depths as shallow as 4500 m below sea level (mbsl) (Stern et al. 2020). These peridotites could have been derived from either forearc (Ohara and Ishii 1998; Michibayashi et al. 2016a) or backarc (Michibayashi et al. 2009; Sato and Ishii 2011) mantle, suggesting that their geological and petrological characteristics may be complicated in relation to the structural evolution of the southern Mariana Trench. In contrast, a few dredge expeditions have been conducted

*Correspondence: michibayashi.katsuyoshi.s5@f.mail.nagoya-u.ac.jp
[2] Department of Earth and Planetary Sciences, Graduate School of Environmental Studies, Nagoya University, Nagoya 464-8601, Japan
Full list of author information is available at the end of the article

to the western side of the Challenger Deep (Hawkins and Batiza 1977; Beccaluva et al. 1980; Fig. 1). Rocks dredged from a small ridge running parallel to the Mariana trench axis on Scripps Institution expedition INDOPAC, Leg 4, in 1976 included a serpentinized peridotite that is highly sheared, so that the "ridge" was thought to be a tectonic sliver of sheared ultramafic rock (Hawkins and Batiza 1977). However, previous studies were limited in scope, and more detailed and extensive geological studies of the mantle peridotites are necessary to understand the tectonic history of the southern Mariana Trench.

In this paper, we present some petrophysical features of newly sampled peridotites from the small ridge on the western side of the Challenger Deep, where Hawkins and Batiza (1977) have found serpentinized peridotites. We tentatively named the small ridge '139°E Ridge'. We show details of their crystallographic fabrics along with other petrological and geochemical data and use these to explain briefly how they have been formed.

2 Geological setting

The Mariana Trench is where the Pacific plate subducts beneath the Philippine Sea plate and its strike changes from N–S in the north to E–W in the south. The Challenger Deep, part of the southern Mariana Trench southwest of Guam, is the deepest trench in the world (Fujioka

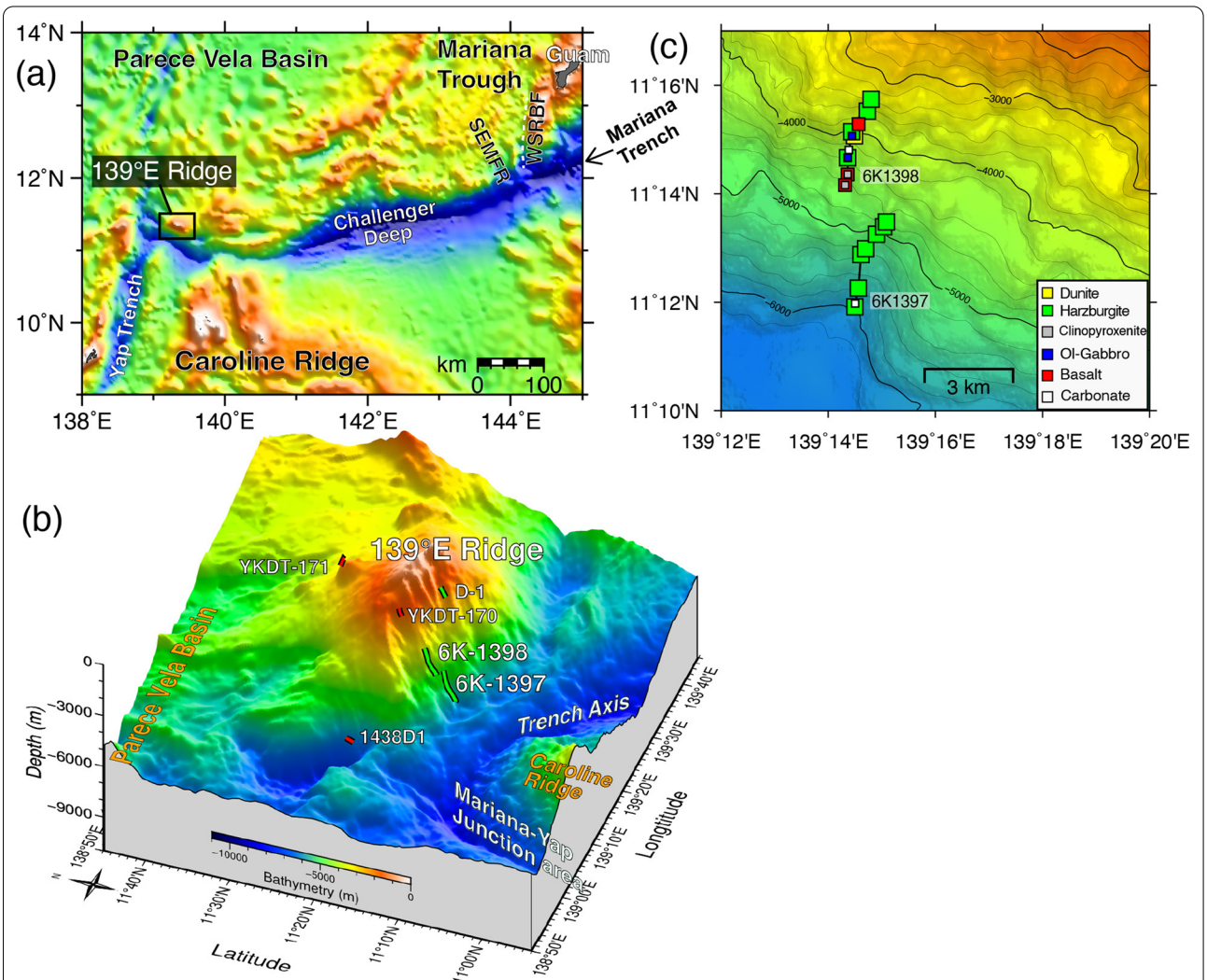

Fig. 1 **a** Bathymetric map of the region around the southern Mariana Trench. SEMFR: Southeast Mariana Forearc Ridge; WSRBF: West Santa Rosa Bank Fault. **b** Three-dimensional perspective view of the 139°E Ridge. *Shinkai 6500* dive tracks (6K-1397 and 6K-1398) are shown by green lines. Deep-tow camera dive tracks (YKDT-170 and YKDT-171) are shown by red lines. D-1 is the dredge line reported by Hawkins and Batiza (1977). 1438D1 is the dredge line reported by Beccaluva et al. (1980). **c** Lithologies recovered along the dive tracks plotted on a bathymetric map. The bathymetric dataset used in each panel is a compilation from the following bathymetric data: ETOPO1, U.S. Extended Continental Shelf Cruise (Armstrong 2010), and Yokosuka ship-board bathymetry

et al. 2002; Fryer et al. 2003). The Mariana forearc narrows markedly along the E–W in the south (Fig. 1a), so that the Mariana trench axis has an arcuate shape due to the collision of the Ogasawara Plateau in the north and the Caroline Ridge in the south (Miller et al. 2006). The southern Mariana Trench from south of Guam to the Yap Trench junction shows a characteristic morphology where the trench axis runs across both the Mariana volcanic arc and a backarc basin (Fig. 1a; e.g., Sleeper et al. 2021). The Mariana and Yap Trenches intersect at a nearly perpendicular angle, forming a typical trench-trench junction (Ohara et al. 2002a; Chen et al. 2019).

The Mariana Arc consists of an active and two fossil volcanic arcs separated by the Parece Vela Basin (29.0–7.9 Ma) and the Mariana Trough (6 Ma to present), both of which are backarc basins (Fig. 1a; Okino et al. 1998; Ohara et al. 2002a, b; Ohara et al. 2003; Tani et al. 2011). The Southeast Mariana forearc rift (SEMFR) is an unusual volcanic rift in the Mariana forearc, which extends from the trench to the southernmost Mariana volcanic arc (Ribeiro et al. 2013a, 2013b). West Santa Rosa Bank Fault (WSRBF) separates older rocks of the Santa Rosa Bank from the SEMFR younger rocks.

3 The 139°E ridge

The study site is located on the southwestern slope of the 139°E Ridge (11°12′N, 139°15′E), which is a small ridge at the southwesternmost tip of the Mariana Trench inner slope at the junction with the Yap Trench (~ 11°20′N, ~ 139°20′E; Fig. 1a, b). Detailed geological surveys of the study area were conducted using the submersible *Shinkai6500* (dives 6K-1397 and 6K-1398) and a deep-tow camera (dives YKDT-170 and YKDT-171) as part of R/V *Yokosuka* cruises in 2014 (Ohara et al. 2015). Each dive site is shown in Fig. 1b, c.

This ridge is ~ 36 km wide and ~ 50 km long, and trends WNW–ESE, parallel to the Mariana Trench to the southwest as reported by Hawkins and Batiza (1977) about the dredge site INDP-04-01 (D-1 in Fig. 1b). The surface shows no corrugation, indicating that this ridge is not an oceanic core complex, as has been identified at slow-spreading mid-ocean ridges (e.g., Cannat et al. 1995; Tucholke et al. 1998; Escartín et al. 2008; MacLeod et al. 2009; Dick et al. 2019; Michibayashi et al. 2019), in the Parece Vela Basin (e.g., Ohara et al. 2001; Harigane et al. 2008, 2010, 2011a, 2011b, 2019; Michibayashi et al. 2014, 2016a, b; Ohara 2016) and in the Shikoku Basin (Basch et al. 2020; Akizawa et al. 2021).

The southwestern slope of the 139°E Ridge differs from the northeastern slope in both bathymetry and geology. The southwestern slope is rugged, whereas the northeastern slope is smooth with small knolls. The northeastern slope is contiguous with the Parece Vela Basin. It is noted that Hawkins and Batiza (1977) dredged serpentinized peridotites from the southwestern slope at depths of 2350–1566 mbsl (D-1 in Fig. 1b).

Several outcrops of plutonic rock were observed on the deeper part of the southwestern slope (Fig. 2a). During our dive surveys, 48 samples (35 peridotites, 2 olivine gabbros, 3 clinopyroxenites, 5 basalts, and 3 carbonates) were recovered at depths of 5999–3430 mbsl (Fig. 1c). Peridotites with varying degrees of serpentinization were found at all sampling sites. Moreover, the YKDT-170 dive revealed that the shallow western part of the ridge (from 1985 to 1740 mbsl) consists of volcanic breccias and carbonate rocks (Fig. 2b). During the YKDT-171 dive, Mn-coated old volcanic rubble was observed covering a small knoll on the northern flank of the ridge (Fig. 2c).

4 Methods

4.1 Petrography

18 peridotite samples have been chosen for our study: 12 from dive 6K-1397 and 6 from dive 6K-1398. In the laboratory, using bleached and saw-cut samples, the foliation and lineation were identified on the basis of the alignment of spinel and pyroxene grains (Fig. 2d, e). Four harzburgites (samples 6K-1397-R03, 6 K-1397-R04, 6K-1397-R08, and 6K-1398-R14) show clear centimeter-scale pyroxene-rich or plagioclase-rich layering parallel to the harzburgite foliation (Fig. 2d, e). We have made thin sections cut perpendicular to the foliation and parallel to the lineation (i.e., XZ sections), except for one dunite sample (6K-1398-R11) for which we did not identify any foliation or lineation. All thin sections were polished using 1 μm diamond paste and colloidal silica for > 5 h for microstructural observations and analyses.

Mineral abundances were determined by microscope point-counting. About 2000 points per thin sections (28 × 48 mm) were measured at 0.2 mm intervals. The minerals identified include both primary minerals such as olivine, orthopyroxene, clinopyroxene, spinel, and plagioclase, and secondary minerals such as serpentine, bastite, and magnetite.

4.2 Crystal-preferred orientations (CPOs)

The crystal-preferred orientations (CPOs) of the olivine and orthopyroxene for harzburgite samples were measured on polished thin sections using a scanning electron microscope equipped with an electron back scatter diffraction (EBSD) system (HITACHI S-3400N with HKL Channel 5) at Shizuoka University (now at Nagoya University). EBSD patterns were produced by interaction between an electron beam and the crystals in thin sections tilted at 70° to the horizontal plane, and indexation of the diffraction patterns was confirmed

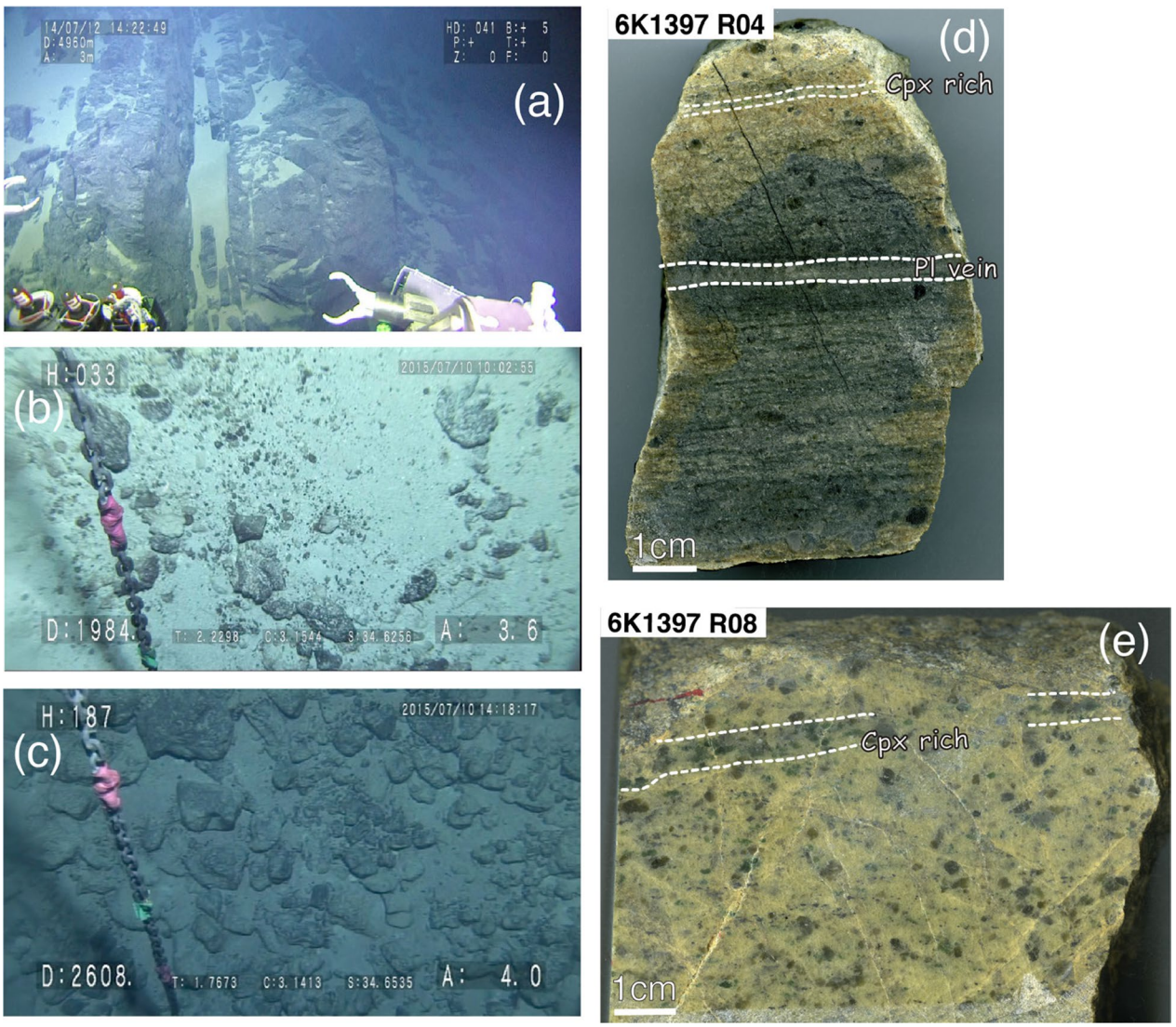

Fig. 2 **a** Peridotite outcrop on the southwestern slope of the 139°E Ridge (4960 mbsl; dive 6K1397). **b** Volcanic and carbonate gravels that cover the shallower part of the southwestern slope of the 139°E Ridge (1984 mbsl; YKDT-170). **c** Mn-coated volcanic rubble covering a small knoll on the northern flank of the 139°E Ridge (2608 mbsl; YKDT-171). **d** Photograph of a saw-cut surface of peridotite sample 6K1397-R04. **e** Photograph of a saw-cut surface of peridotite sample 6K1397-R08

manually for each orientation. We determined the crystal orientations of ~200 olivine grains and ~100 orthopyroxene grains as one point per grain, and visually checked the computerized indexation of each diffraction pattern.

To characterize the CPOs, we determined the fabric strength and distribution density of the principal crystallographic axes. We used the *J*-index (Mainprice and Silver 1993) to quantify the intensity of a given CPO. The *J*-index has a value of unity for a random distribution and a value of infinity for a single crystal (Mainprice and Silver 1993; Michibayashi and Mainprice 2004). The fabric strength was also determined using the *M*-index technique (Skemer et al. 2005). Using this approach, the distribution of random-pair misorientation angles of a sample (Wheeler et al. 2001) is compared with the distribution of misorientation angles from a theoretical random fabric. The *M*-index is scaled from zero to one, where $M=0$ represents a random fabric and $M=1$ represents a single crystal. In addition, we also computed the *pfJ* index. The *pfJ* index has a value of unity for a random distribution and a maximum value for olivine of ~ 60 for a single crystal of olivine. In the present case of olivine, the [100], [010], and [001] axes are all two-fold rotation axes,

meaning that the *pfJ* values can be directly compared. *pfJ* values are useful to compare intensities among pole figures of the three axes along with contours in individual samples. We calculated the *J*, *pfJ*, and *M*-index values using MTEX Toolbox (v 5.8.0) for MATLAB®.

4.3 P-wave velocities estimated from the olivine CPOs and *Vp*-Flinn diagram

A single crystal of olivine contains intrinsic elastic anisotropies. Therefore, olivine aggregates have characteristic seismic properties in accordance with the distribution of crystallographic axes. For quantifying CPOs, the P-wave velocities of a virtual olivine aggregate were estimated from the crystallographic orientation data measured by EBSD and the elastic property of a single crystal of olivine (Abramson et al. 1997) using the MTEX Toolbox (v. 5.8.0) for MATLAB® (Mainprice et al. 2011). Since P-wave velocities can be calculated in all directions, the V_P anisotropy (AV_P) is given by

$$AV_P = 200 \times \frac{V_1 - V_3}{V_1 + V_3}, \tag{1}$$

where V_1 and V_3 are the maximum and minimum velocities, respectively.

Olivine CPO types were quantified using the V_P-Flinn Diagram (Michibayashi et al. 2016a, b). The angle of inclination between the point of origin (1, 1) and a point in the Flinn diagram can be used as a quantitative measure of the olivine CPO pattern, which was introduced as the Fabric-Index Angle (FIA) by Michibayashi et al. (2016a), as follows:

$$\text{Fabric Index Angle} = \tan^{-1}\left(\frac{\frac{V_x}{V_y} - 1}{\frac{V_y}{V_z} - 1}\right). \tag{2}$$

By using the V_P structure of a virtual olivine aggregate as a framework, V_X, V_Y, and V_Z can be rephrased to V_1, V_2, and V_3, respectively. We use three P-wave velocities (V_1, V_2, and V_3) in a Flinn diagram with V_2/V_3 for the horizontal axis and V_1/V_2 for the vertical axis, and the origin at (1, 1). The Fabric-Index Angle, using variable V_1, V_2, and V_3, can be used to determine whether the olivine fabric is AG type, D type, or a point maximum A type (see also Kakihata et al. 2022).

4.4 Major element compositions

The major element compositions of olivine, orthopyroxene, clinopyroxene, spinel, and plagioclase were measured using an electron probe micro-analyzer (EPMA: JEOL JXA-8900R) at Shizuoka University, Japan. The operating conditions were an accelerating voltage of 20 kV, a specimen current of 12 nA, and a beam diameter of 5 μm. Natural and synthetic JEOL mineral standards were used for data calibration. The X-ray peak of Ni was counted for 30 s, whereas those of the other elements were counted for 20 s. The conventional ZAF matrix correction was used. The Fe^{3+} contents of spinel were calculated on the basis of stoichiometry.

We estimated temperature conditions assuming a pressure of 15 kbar and using the Ol–Sp thermometer established by Ballhaus et al. (1990) as follows:

$$\begin{aligned} T = (&6530 + 280P + 7000 + 108P * \left(1 - 2X_{\mathrm{Fe}}^{ol}\right) - 1960 \\ &* \left(X_{\mathrm{Mg}}^{sp} - X_{\mathrm{Fe}^{2+}}^{sp}\right) + 16150 * X_{\mathrm{Cr}}^{sp} + 25150 \\ &* \left(X_{\mathrm{Fe}^{3+}}^{sp} + X_{\mathrm{Ti}}^{sp}\right) / \left(R \ln K_{D^{\mathrm{Mg-Fe}}}^{ol-sp} + 4.705\right), \end{aligned} \tag{3}$$

where T is in K; X_{Fe}^{ol} is the $Fe^{2+}/(Fe^{2+} + Mg)$ ratio in olivine; $X_{\mathrm{Fe}^{2+}}^{sp}$, X_{Cr}^{sp}, and $X_{\mathrm{Fe}^{3+}}^{sp}$ are the values of $Fe^{2+}/(Fe^{2+} + Mg)$, $Cr/(Fe^{3+} + {}^{\mathrm{VI}}Al + Ti + Cr)$, and $Fe^{3+}/\sum Fe$ in spinel, respectively; X_{Ti}^{sp} is the number of Ti cations in spinel on the basis of 4 oxygens; and $K_{D^{\mathrm{Mg-Fe}}}^{ol-sp}$ is the ratio $(X_{\mathrm{Fe}}^{ol} * X_{\mathrm{Fe}^{3+}}^{sp})/(X_{\mathrm{Fe}}^{ol} * X_{\mathrm{Mg}}^{sp})$.

Oxygen fugacity was calculated from coexisting olivine and spinel compositions using the oxygen barometer of Ballhaus et al. (1990) as follows:

$$\begin{aligned} \Delta log\left(f_{O_2}\right)^{\mathrm{FMQ}} = &0.27 + \frac{2505}{T} - 400\frac{P}{T} - 6\log\left(X_{\mathrm{Fe}}^{ol}\right) \\ &- \frac{3200\left(1 - X_{\mathrm{Fe}}^{ol}\right)^2}{T} + 2\log\left(X_{\mathrm{Fe}^{2+}}^{sp}\right) \\ &+ 4\log\left(X_{\mathrm{Fe}^{3+}}^{sp}\right) + 2630\frac{\left(X_{\mathrm{Al}}^{sp}\right)^2}{T}, \end{aligned} \tag{4}$$

where P is in GPa, T is in K, and X_{Al}^{sp} is the $Al/(Fe^{3+} + {}^{\mathrm{VI}}Al + Ti + Cr)$ ratio in spinel.

4.5 Trace element compositions

Rare earth element (REE) and trace-element contents of clinopyroxene and orthopyroxene in harzburgite samples were determined using laser ablation-inductively coupled plasma-mass spectrometry (Thermo Scientific Element XR) at Academia Sinica, Taiwan. ^{43}Ca was used as an internal standard for data reduction based on elemental concentrations obtained by EPMA. NIST SRM 612, BHVO-1, and BCR-1 were used as external calibration standards and were analyzed at the beginning of each batch of no more than 12 unknowns. NIST SRM 612 was analyzed again at the end of each batch. The diameter of ablation spots was 60 μm. After each analysis, data reduction was carried out using GLITTER software (Griffin et al. 2008).

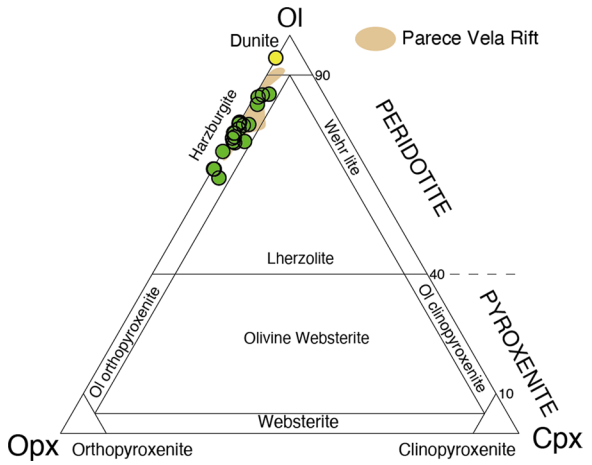

Fig. 3 IUGS ternary classification plot for peridotites showing lithological types found in the 139°E Ridge. The field for the Parece Vela Basin is shown by orange domain after Ohara et al. (2003)

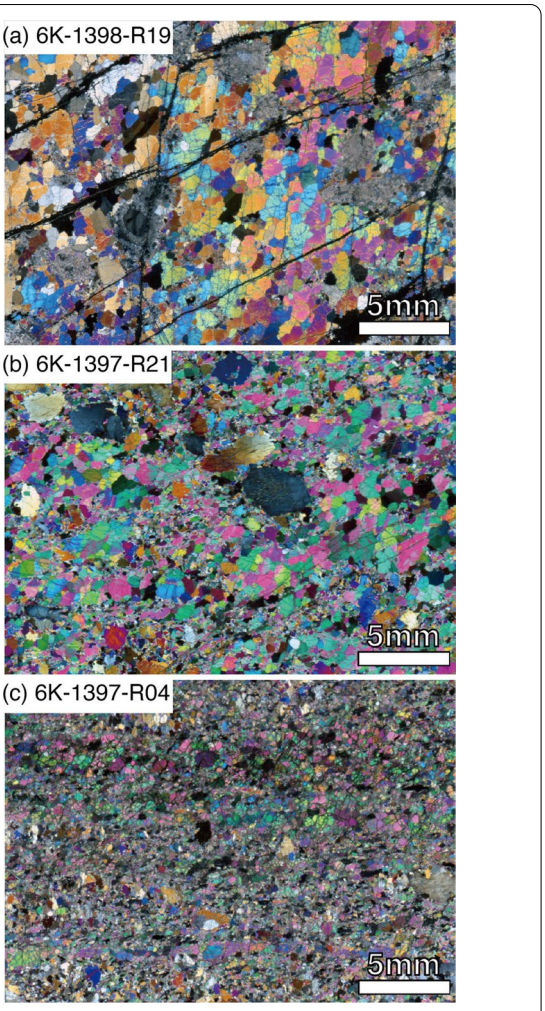

Fig. 4 Photomicrographs (cross-polarized light) of representative peridotites from site 1 on XZ section. **a** Coarse-grained texture. **b** Heterogeneous intermediate texture. **c** Fine-grained texture

5 Results

5.1 Modal compositions

The peridotites consist of harzburgite and dunite. Results of the modal compositions are shown in Additional file 1: Table S1. Modal abundances of olivine range from 61.1 to 83.0%, and those of orthopyroxene and clinopyroxene range from 11.5 to 32.5% and 0 to 3.4%, respectively. Abundances of spinel range from 0.1 to 3.2%, whereas those of plagioclase range from 0 to 5.7%. These modal data were subsequently re-calculated to estimate the modal compositions of primary minerals in the peridotite, so that mesh-textured serpentine and associated magnetite were assigned to olivine, bastite and associated talc were assigned to orthopyroxene, and bastite with clinopyroxene relics was assigned to clinopyroxene. Magnetite at the margins of spinel was assigned to spinel. The re-calculations show that the 18 peridotites include 17 harzburgites and 1 dunite (Fig. 3).

5.2 Peridotite textures

The peridotites can be subdivided according to their textures, even though pyroxenes were altered to bastite in three samples (6K-1397-R01, 6K-1397-R05, and 6K-1398-R19). Clinopyroxene and plagioclase are heterogeneously distributed in hand specimens (Fig. 2d, e), and the textures vary from coarse-grain size (> 1 mm) to fine-grain size (< 0.5 mm) as well as heterogeneous intermediate textures consisting of both fine and coarse grains (Fig. 4).

Two coarse-grained harzburgite samples (6K-1398-R15 and R19) were sampled from the shallowest part of the 139°E Ridge (3705–4042 mbsl) and are characterized by coarse (up to 1 mm) equigranular olivine grains. Olivine shapes may be interlobate (Fig. 5a; 6K-1398-R15) or polygonal (6K-1398-R19). Polygonal olivine grains show weak shape-preferred orientations perpendicular to spinel foliation. Orthopyroxene grains have irregular grain boundaries and are more-or-less equidimensional with no shape-preferred orientation (Fig. 5b). Clinopyroxene grains show similar textures to orthopyroxene, although their occurrences are minor.

Twelve harzburgite and one dunite samples have heterogeneous intermediate textures that are characterized by heterogeneous distributions of both coarse and fine olivine grains. Coarse olivine grains show undulose extinction and kink bands (Fig. 5c). In general, olivine grains show polygonal textures with triple junction grain boundaries (Fig. 5d). Orthopyroxenes show undulose extinction.

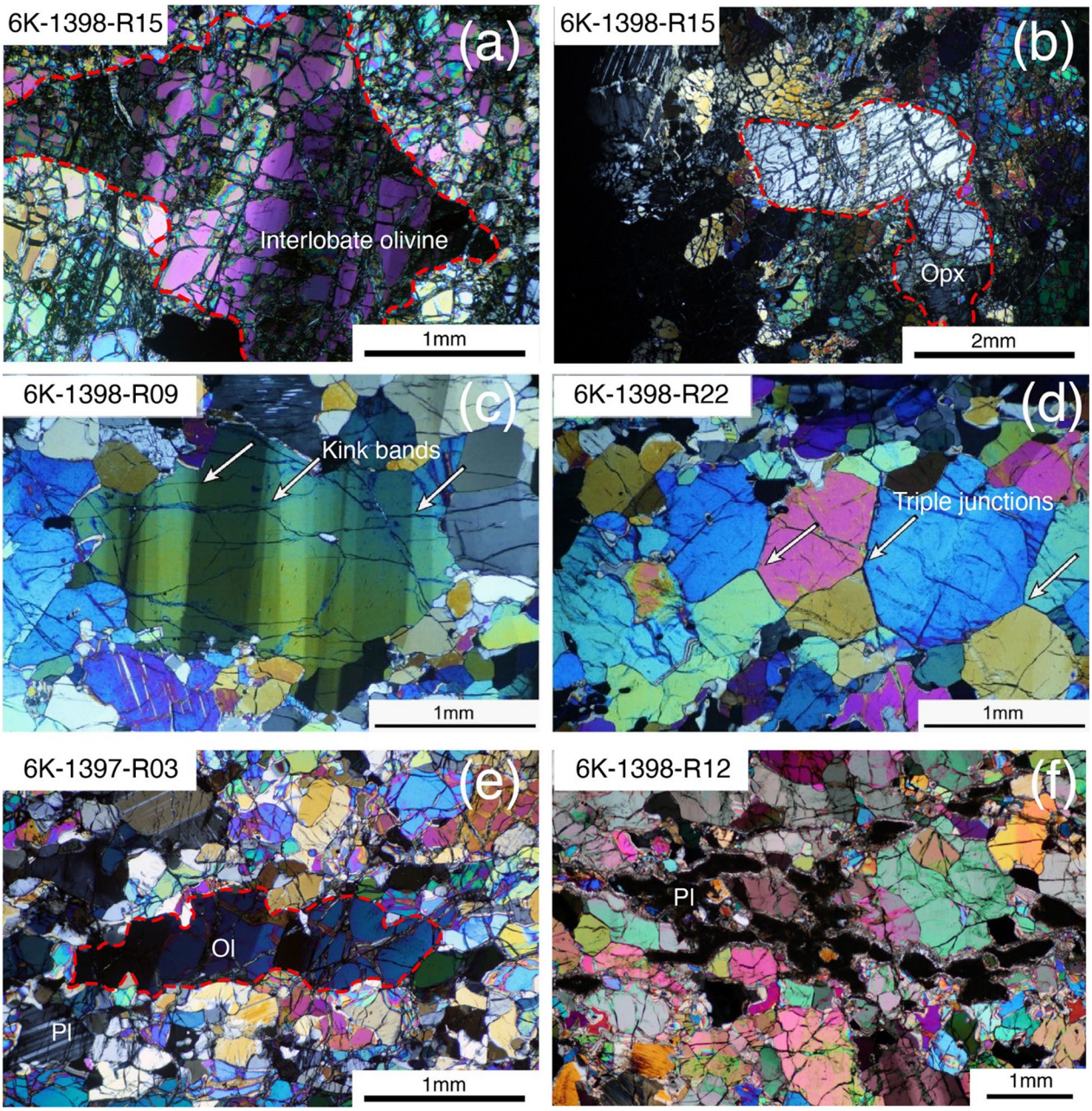

Fig. 5 Photomicrographs of 139°E Ridge peridotites under cross-polarized light. The long side of each photomicrograph is parallel to the lineation. **a** Coarse-grained texture showing interlobate olivine. **b** Coarse-grained texture with irregularly shaped orthopyroxene (Opx). **c** Heterogeneous texture showing coarse olivine grains with undulose extinction and kink bands. **d** Heterogeneous texture showing olivine grains with polygonal textures and triple junctions. Pl: plagioclase. **e** Fine-grained texture showing a larger olivine with serrated grain boundaries (Ol) that is elongate parallel to the lineation. **f** Fine-grained texture showing grain boundaries in an orthopyroxene porphyroclast. Pl: plagioclase that appears as altered phases as irregular diffuse dark brown patches of hydrogrossular

Three fine-grained harzburgite samples (6K-1397-R02, -R03, and -R04) were obtained from the deepest site (Site 1, 5999 mbsl). The rocks are characterized by small olivine grains, ca. 0.2–0.5 mm across. Coarser olivine grains are elongate parallel to the lineation and show serrated grain boundaries (Fig. 5e). Plagioclase appears as fresh interstitial grains (Fig. 5e) or altered phases as irregular diffuse dark brown patches of hydrogrossular (Fig. 5f).

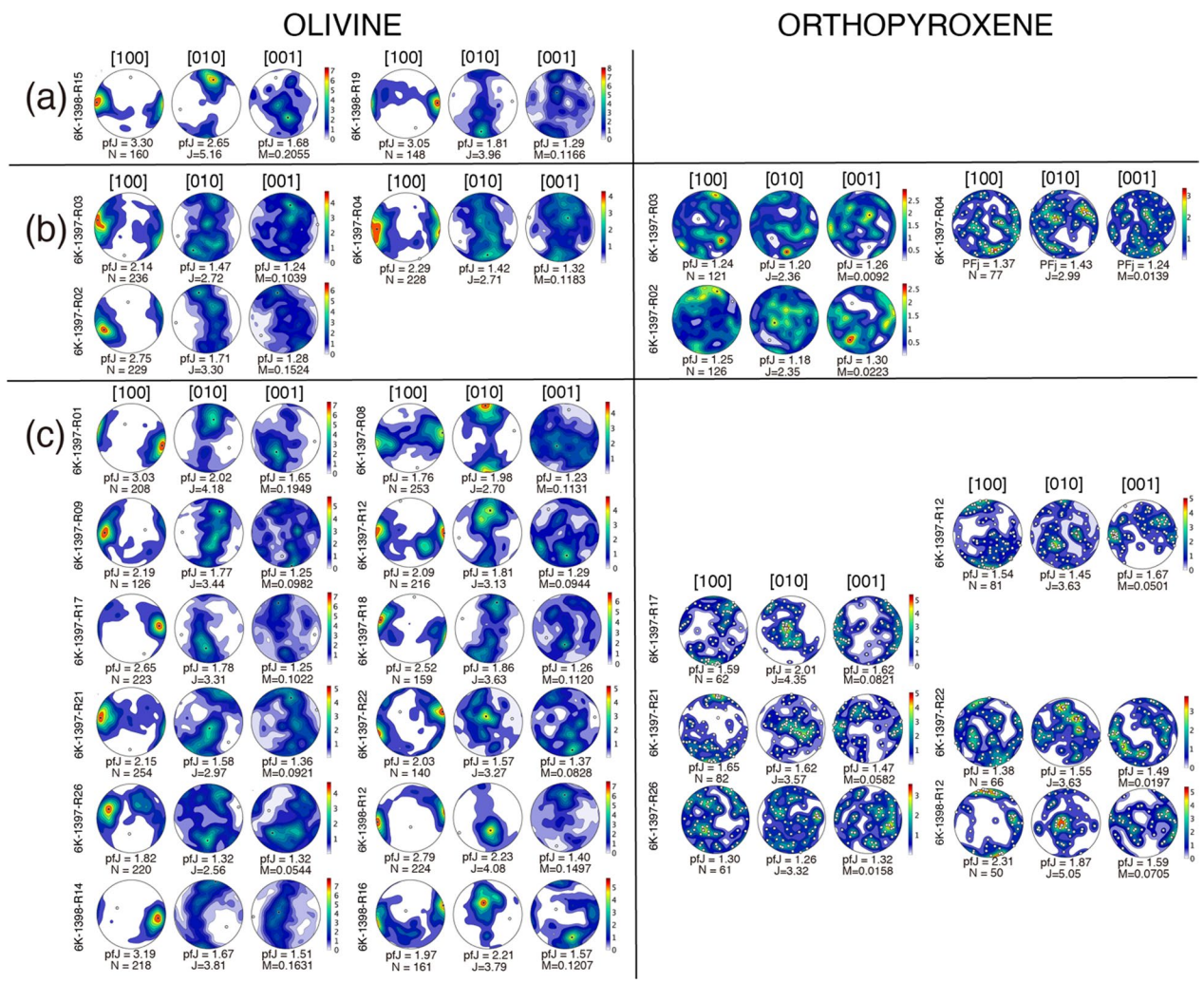

Fig. 6 Olivine and orthopyroxene crystal-fabric data for peridotites from the 139°E Ridge plotted on equal-area, lower-hemisphere projections. Contours are in multiples of uniform distribution. Half widths are 10°. One measurement per grain. In orthopyroxene CPOs comprising fewer than 100 grains, individual grains are shown as a white circle, whereas those less than 50 grains are excluded as they are too small numbers to present CPOs. N is the number of grains measured. J is the *J*-index. M is the *M*-index. pfJ is *pfJ*-index. **a** Coarse-grained texture. **b** Fine-grained texture. **c** Heterogeneous textured rocks

5.3 CPOs

Olivine CPOs and the *Vp*-Flinn diagram with CPO data for the harzburgite samples are shown in Figs. 6 and 7, respectively. Calculated values related to olivine crystal-fabrics are listed in Additional file 1: Table S2. For fabric intensities, the *J*-index values ranged from 2.56 to 5.16 and *M*-index values ranged from 0.0544 to 0.2055. Calculated AV_P values range from 6.83 to 13.22% (Additional file 1: Table S2). The coarse-grained harzburgite (6K-1398-R15) has the highest fabric intensity among all samples with the intense [100] concentrations parallel to the lineation (i.e., *pfJ* of [100]: 3.30, *J*-index: 5.16, *M*-index: 0.2055).

The Fabric-Index Angle (FIA), which is about impartially determining the olivine crystal-fabric types, ranged from 35.7° to 89.7°. Various olivine crystal-fabrics occurred related to their grain sizes. Two coarse-grained textures (6K-1398-R15 and R19) correspond to strong A-type (010)[100] patterns (FIA: 57.8–58.3, AV_P: 11.1%–13.2%, *J*-index: 3.96–5.16, *M*-index: 0.1166–0.2055) (Fig. 6a), three fine-grained textures (6K-1397-R02, -R03, and -R04) correspond to D-type {0kl}[100] patterns (FIA: 79.1–89.7, AV_P: 9.12–11.33%, *J*-index: 2.71–3.30, *M*-index: 0.1039–0.1524)(Fig. 6b), and 12 heterogeneous textures correspond to a mix of A-type (010)[100], D-type {0kl}[100] and various indistinct patterns (FIA:

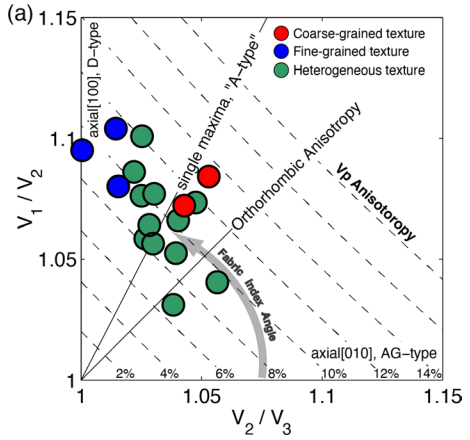

Fig. 7 V_P-Flinn diagram for the 139°E Ridge peridotites. Red symbols indicate coarse-grained texture, blue symbols indicate fine-grained texture, and green symbols indicate samples with heterogeneous texture

35.7–75.9, AV_P: 6.83–12.09%, *J*-index: 2.56–4.18, *M*-index: 0.0544–0.1949) (Fig. 6a).

Orthopyroxene CPOs are also shown in Fig. 6. The *J*-index values ranged from 2.35 to 5.05 and M-index ranged from 0.0092 to 0.0821, although the number of grains measured are mostly less than 100. A few heterogeneous textures correspond to (100)[001] patterns such as 6K-1397-R21 and 6K-1398-R12, whereas fine-grained textures correspond to indistinct patterns with weak fabric intensities. We do not present any data for the patterns of orthopyroxenes in the coarse-grained texture because of the small number of measurements.

5.4 Major element compositions of the minerals

The Mg# ($=Mg^{2+}/(Mg^{2+}+Fe^{2+})$) of olivine in the peridotites range from 0.90 to 0.92 (Additional file 1: Tables S3, S4). NiO contents range from 0.36 to 0.41 wt.% in the harzburgites, and the NiO content of the dunite is 0.36 wt.%. The relationships between olivine Mg# and spinel Cr# ($=Cr^{3+}/(Cr^{3+}+Al^{3+})$) are shown in Fig. 8a. Orthopyroxene Mg# range from 0.90 to 0.92 (Additional file 1: Tables S5, S6). The Al_2O_3 contents of the harzburgite orthopyroxene range from 2.21 to 3.04 wt.%. Clinopyroxene Mg# range from 0.92 to 0.93, and the Al_2O_3 contents of harzburgite clinopyroxene range from 2.53 to 3.85 wt.% (Additional file 1: Tables S7, S8). The An values of plagioclase are 93–98 (Additional file 1: Tables S9, S10).

The values of spinel Cr# and Mg# in the peridotites range from 0.36 to 0.57 and 0.52 to 0.68, respectively (Fig. 8b; Additional file 1: Tables S11, S12). TiO_2 contents of harzburgite spinel range from 0.07 to 0.45 wt.%, and the TiO_2 content of the dunite spinel is 0.13 wt.% (Fig. 8c). The values of Y_{Fe} ($=Fe^{3+}/(Cr^{3+}+Al^{3+}+Fe^{3+})$) of harzburgite spinel range from 0.0250 to 0.0743 (Fig. 8e).

The temperatures we estimated, assuming a pressure of 15 kbar and using the Ol–Sp thermometer of Ballhaus et al. (1990), range from 637 to 749 °C (Fig. 10; Additional file 1: Tables S11, S12). Subsequently, the values of $\Delta\log(f_{O_2})^{FMQ}$ we calculated, assuming a pressure of 15 kbar with estimated temperatures, range from −0.42 to 0.92 (Fig. 8d; Additional file 1: Tables S11, S12), which is higher than those of abyssal peridotites (-1.20 ± 0.64; Bryndzia and Wood 1990) but in the range of arc-peridotites (Parkinson and Arculus 1999).

5.5 Trace element compositions of the pyroxenes

The results of the clinopyroxene analyses are shown in Additional file 1: Table S13. Primitive-mantle-normalized incompatible element patterns for clinopyroxene are shown in Fig. 9a, b, and chondrite-normalized REE patterns are shown in Fig. 9c. The patterns exhibit steepening slopes from the middle to the light REEs. Nb and Zr show positive and negative anomalies relative to the LREEs, respectively.

The results of orthopyroxene analyses are listed in Additional file 1: Table S14. Primitive-mantle-normalized incompatible element patterns for orthopyroxene are shown in Fig. 9d. The patterns slope down from the HREEs to the LREEs. There are positive anomalies of Ti, Hf, and Nb.

6 Discussion

The shallow (from 1985 to 1740 mbsl) western part of the 139°E Ridge consists of volcanic breccias and carbonate rocks (YKDT-170 in Fig. 1b), whereas Hawkins and Batiza (1977) have found serpentinized peridotites at the similar depth (D-1 in Fig. 1b). Moreover, Mn-coated volcanic rubble was observed at a small knoll on the northern flank of the ridge (YKDT-171 in Fig. 1b). In contrast, the deeper (5999 to 3430 mbsl) part of the southwestern slope consists dominantly peridotites along with some volcanic rocks and carbonates (Fig. 1b, c), suggesting that the 139°E Ridge could consist of the shallower basaltic crust and the deeper mantle peridotites in a cross section (Fig. 11). Moreover, Crawford et al. (1986) suggested that some samples from the deepest north-western flank of the ridge (1438D1 in Fig. 1b) may represent backarc basin affinity of the initial stage of the Mariana Trough opening, as Beccaluva et al. (1980) have obtained ~ 7.8 Ma in age from the volcanic rocks. It suggests that the 139°E Ridge could be abruptly terminated on the west by a tectonic boundary such as a fault. Here, we use our new data to explore

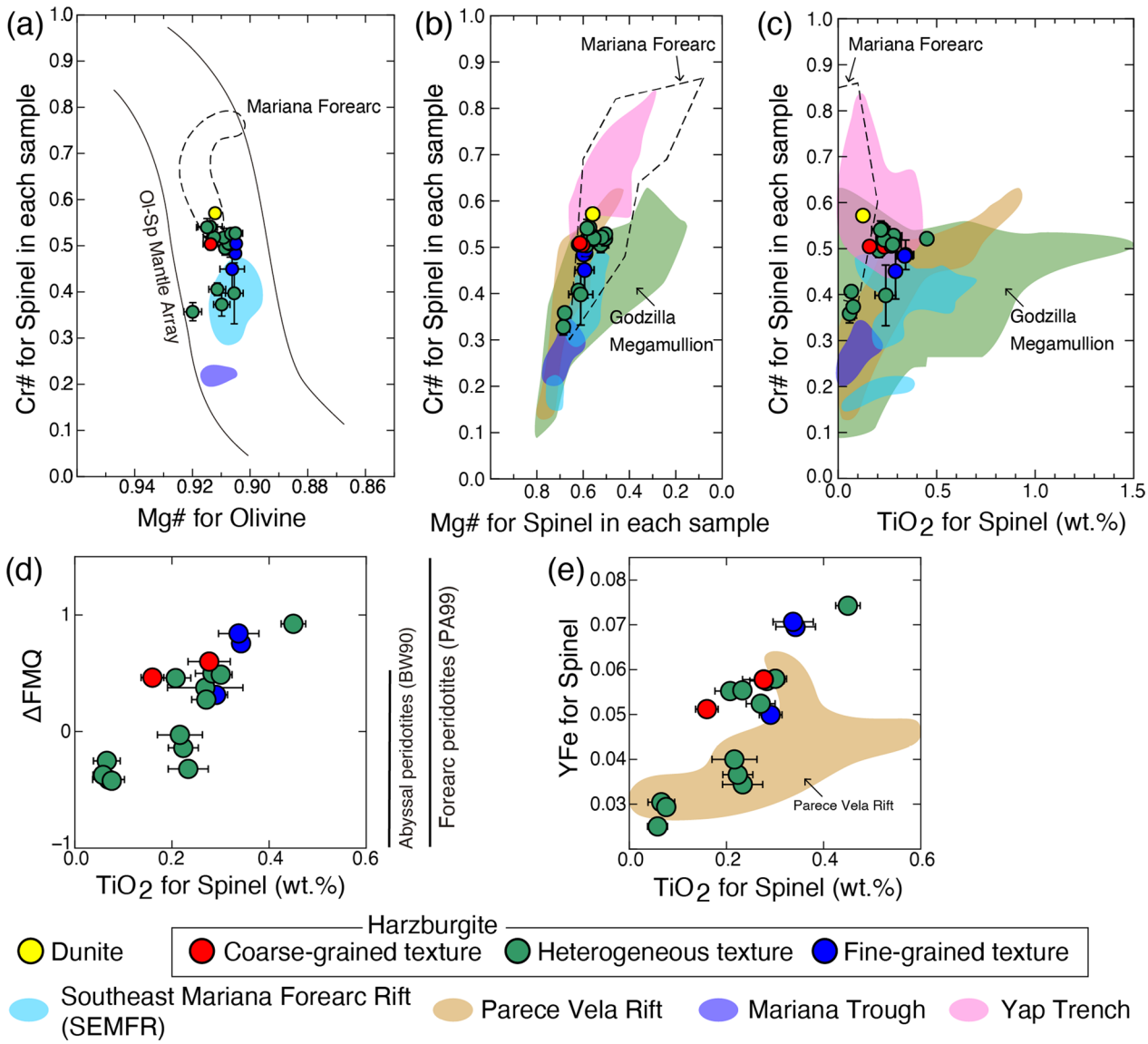

Fig. 8 Compositional data for dunite (red) and harzburgite (green). Error bar is the deviation of average values. Green filled circles indicate harzburgite, and red filled circles indicate dunite. **a** Average Mg# of olivine vs. average Cr# of spinel in the 139°E Ridge peridotites. The region between the two solid lines is the olivine–spinel mantle array (OSMA), where mantle-derived spinel peridotites plot (Arai 1994). **b** Average Mg# vs. average Cr# for spinel grains in the 139°E Ridge peridotites. **c** Average TiO_2 values vs. average Cr# for spinels in the 139°E Ridge peridotites. **d** Average TiO_2 contents of spinel vs. ΔFMQ values for the 139°E Ridge peridotites. ΔFMQ values were calculated from the major element compositions of olivine and spinel (Ballhaus et al. 1990). ΔFMQ values for abyssal peridotites (Bryndzia and Wood 1990) and forearc peridotites (Parkinson and Arculus 1999) are shown in the vertical lines. **e** Average TiO_2 values vs. Y_{Fe} values for spinel in the 139°E Ridge harzburgites. The compositional field for the Godzilla Megamullion is shown by green domain (Loocke et al. 2013), the field for the Parece Vela Basin is shown by orange domain (Ohara et al. 2003), the field for the Mariana Trough is shown by blue domain (Ohara et al. 2002a), the field for the "Mariana Trough" outcropped in Mariana Trench is shown by cyan domain (Michibashi et al. 2009), the field for the Yap Trench is shown by magenta domain (Ohara et al. 2002b; Chen et al. 2019), and the field for the Mariana forearc is shown by a dashed line (Ishii et al. 1992; Ohara and Ishii 1998)

following two questions: (1) What was the origin of peridotites in the 139°E Ridge? and (2) What is the dominant olivine crystal-fabric type in these peridotites and how were these modified by structural development of the 139°E Ridge?

6.1 Origin of the 139°E Ridge peridotites

The western side of the Challenger Deep is bounded by the 139°E Ridge. The ridge is located at the westernmost tip of the Mariana forearc as well as at the southern tip of the Parece Vela Rift. Therefore, it is not clear whether the

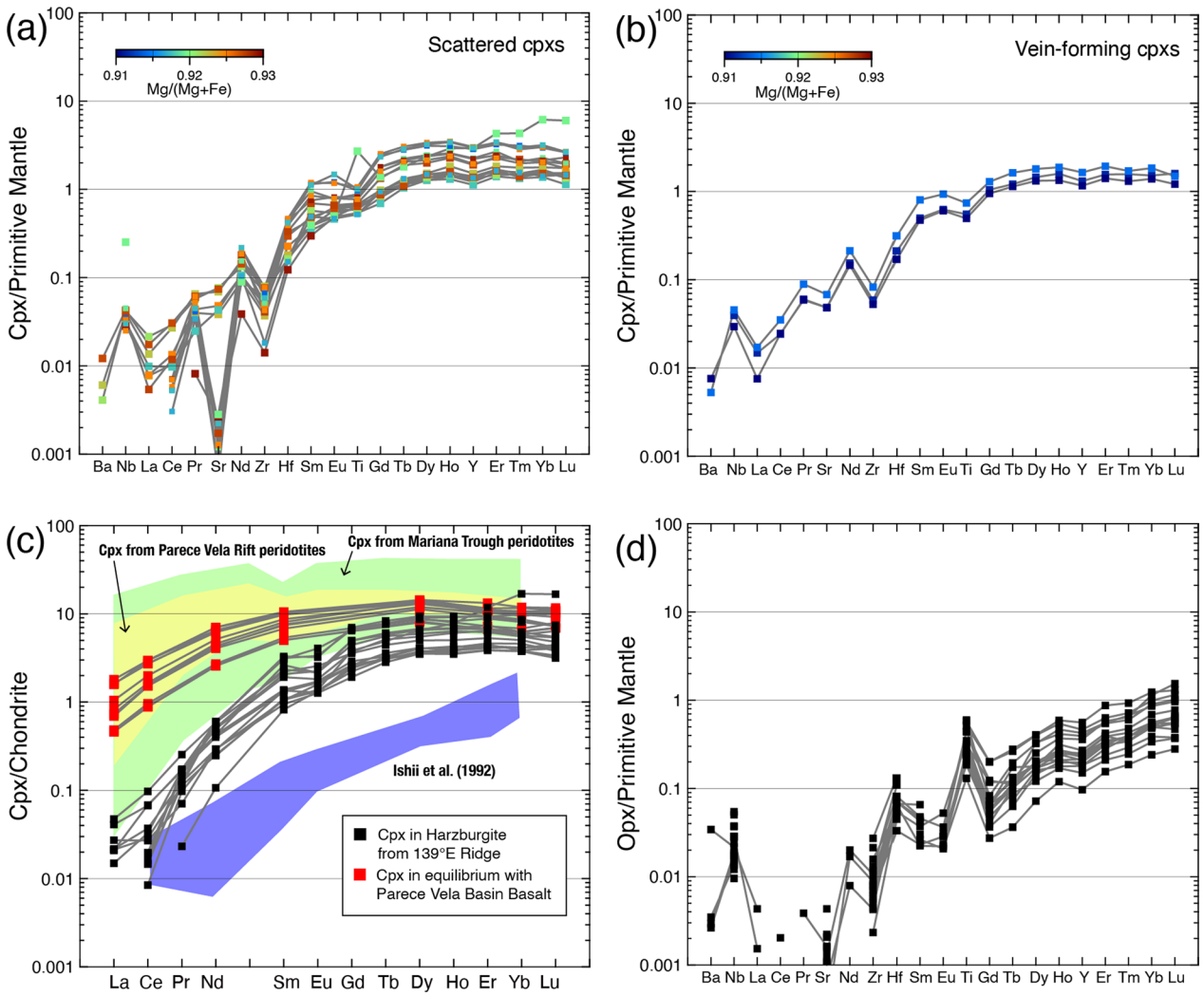

Fig. 9 Primitive-mantle-normalized incompatible element patterns for **a** scattered clinopyroxenes and **b** vein-forming clinopyroxenes in the 139°E Ridge peridotites. The colors indicate the Mg# values of clinopyroxene. Primitive mantle values are from McDonough and Sun (1995). **c** Chondrite-normalized rare earth element patterns for clinopyroxenes. Chondrite values are from Anders and Grevesse (1989). Black dots indicate clinopyroxenes of the 139°E Ridge peridotites. Red dots indicate calculated clinopyroxenes in equilibrium with Parece Vela Basin basalt (Ishizuka et al. 2010). Yellow field is clinopyroxene from Parece Vela Rift peridotites (Ohara et al. 2003), whereas green field is clinopyroxene from Mariana Trough peridotites (Ohara et al. 2002a, b). The blue field is clinopyroxene from Mariana forearc (Ishii et al. 1992). The partition coefficients between clinopyroxene and melt are from Hart and Dunn (1993). **d** Primitive-mantle-normalized incompatible element patterns for orthopyroxenes of the 139°E Ridge peridotites. Primitive mantle values are from McDonough and Sun (1995)

peridotites exposed on the ridge were derived from the Mariana forearc or from the mantle of the Parece Vela Basin.

The relationships between spinel Cr# and olivine Mg# are consistent with the olivine–spinel mantle array (OSMA; Fig. 8a; Arai 1994), showing that the peridotites are exposed mantle. Spinel Cr# is generally an indicator of the degree of melting and melt-peridotite reaction, since spinel Cr# correlates with the degree of melting (Dick and Bullen 1984; Keleman et al. 1992). Chemical compositions of spinel in our samples are similar to those of the Parece Vela Rift peridotites (Ohara et al. 2003; Loocke et al. 2013) rather than those of Mariana forearc peridotites (Ishii et al. 1992; Ohara and Ishii 1998) (Fig. 8b, c), suggesting that the peridotites were derived from a relatively fertile mantle with spinel Cr# as low as 0.36. Ti contents can record the influence of trapped or transient MORB-like melts (Dick and Bullen 1984). The elevated TiO_2 contents at medium values of Cr# (~0.5) of the harzburgite spinel and presence of interstitial plagioclase are characteristics, like those of Parece Vela Rift peridotites (Fig. 8c), suggesting that melt reacting with

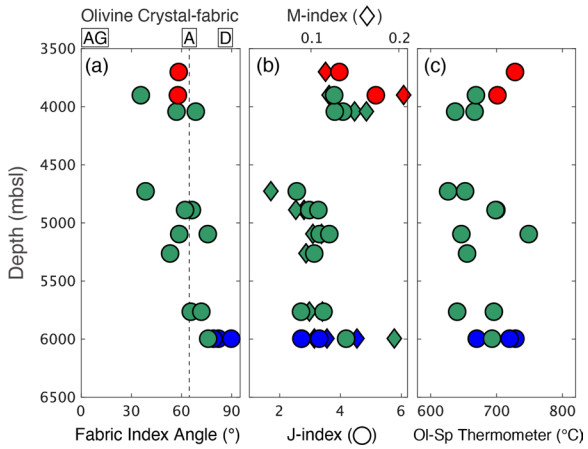

Fig. 10 Spatial trends in olivine crystal-fabric type, crystal-fabric intensity and estimated temperature for the 139°E Ridge along the *Shinkai 6500* dive track. Red symbols indicate coarse-grained samples, green symbols indicate samples with heterogeneous textures, and blue symbols indicate fine-grained samples. **a** FIA vs. depth. AG: AG type olivine crystal-fabric, A: A type olivine crystal-fabric, D: D type olivine crystal-fabric. **b** Fabric intensity (*J*-index and *M*-index vs. depth. **c** Estimated temperatures (Ol–Sp thermometer) vs. depth

the peridotites would be compositionally compatible with Parece Vela Basin basalts. Moreover, our peridotite samples show a heterogeneous distribution of clinopyroxene (Fig. 2), and these form veins in sample 6K-1397-R08. The trace element patterns for clinopyroxene are similar regardless of their occurrence, indicating a common origin (Fig. 9a, b). Their middle to heavy REE contents are more depleted than those of the Parece Vela Basin peridotites (Ohara et al. 2003) but are more fertile than those of the Mariana forearc peridotites (Ishii et al. 1992) (Fig. 9c). It is noted that several clinopyroxene patterns show strongly negative Sr anomalies, which are probably related to the presence of plagioclase, which has a high partition coefficient compared to clinopyroxene (Blundy and Wood 1994). These mineralogical and geochemical features could result from melt-rock interactions under conditions of the shallow lithospheric mantle. As a result, although the 139°E Ridge peridotites were collected from the Mariana Trench inner slope (Fig. 1a–c), we argue that the 139°E Ridge peridotites had been formed in a tectonic environment such as a back-arc basin rather than a subduction initiation/forearc environment, so that the Parece Vela Basin mantle could be exposed on the southwestern slope of the 139°E Ridge (Fig. 1b).

Hellebrand et al. (2002) established the following equation for the degree of melting:

$$F = 10 \ln (\text{Spinel Cr\#}) + 24, \quad (5)$$

where F is the degree of fractional melting (%). Accordingly, the degrees of melting of the uppermost mantle are estimated to have been ~ 15%, using plagioclase free samples.

Spinel Ti contents correlate with the redox state (Y_{Fe} and ΔFMQ) (Fig. 8d, e), and such a correlation has been documented for the Parece Vela Basin peridotites by Ohara et al. (2003). The values of ΔFMQ are higher than those of abyssal peridotites but in the range of arc-peridotites (Fig. 8d). Since the oxidizing condition of the mantle could have resulted from a hydrous environment

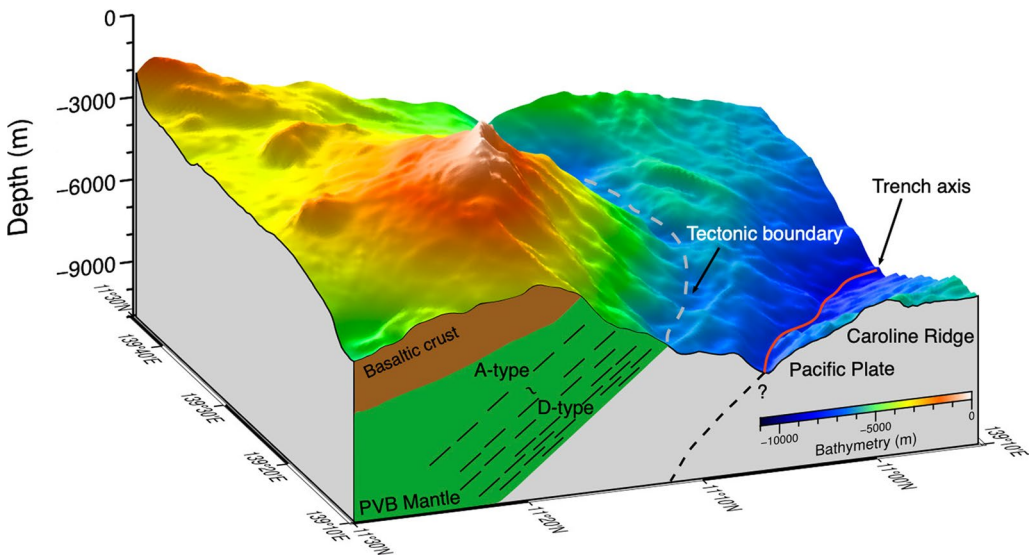

Fig. 11 Schematic bathymetry with a presumed cross section of the 139°E Ridge

(Sato 1978), peridotites with high-TiO_2 spinel may have been oxidized by basaltic melt.

6.2 Dominant fabric type and its modification by structural development of the 139°E Ridge

Detailed geological surveys using the submersible *Shinkai6500* (dives 6 K-1397 and 6 K-1398) revealed that the fresh peridotites occur on the 139°E Ridge. Peridotites on the 139°E Ridge show somehow systematic textural variations as a function of their exposed depths. Coarse-grained peridotites have been found from the shallowest sites (3705–4042 mbsl), whereas fine-grained peridotites occur at the deepest site (5996 mbsl) (Fig. 10a, b). These textural variations could have resulted from various deformation conditions such as deformation at near-solidus temperatures for the coarse-grained peridotites and ductile shearing at lower temperatures for the fine-grained peridotites (e.g., Nicolas and Poirier 1976; Michibayashi and Mainprice 2004).

There is a relationship between olivine crystal-fabrics and their textures. A-type crystal-fabrics occur in coarse-grained peridotites (Fig. 10a), and this is consistent with experimental studies demonstrating that (010)[100] slip system is the most active among {0kl}[100] slip systems under the highest-temperature conditions (e.g., Nicolas et al. 1973; Avé Lallemant et al. 1975; Zhang and Karato 1995). Therefore, the A-type crystal-fabrics in the coarse-grained peridotites on the 139°E Ridge may represent the dominant fabric of the lithospheric mantle below the Parece Vela Basin.

The peridotites with fine-grained textures from the deepest site on the ridge show higher FIA values for their D-type crystal-fabrics than the other harzburgites (Fig. 10a, b). Since D-type crystal-fabrics are considered to result from deformation under relatively higher flow stresses than those for A-type crystal-fabrics (Mainprice and Nicolas 1989; Jung et al. 2006; Michibayashi et al. 2006), a ductile shear zone could occur in the deepest part of the 139°E Ridge (Fig. 11). Therefore, the 139°E Ridge may have been uplifted along an underlying ductile shear zone, where the Caroline Ridge collided with the southern Mariana forearc (Altis 1999; Miller et al. 2006). It is likely that the development of a ductile shear zone in the deepest part of the ridge would have been induced by this collision (Fig. 11).

The temperatures ranged from ca. 600–750 °C, regardless of textures and sampling depths (Fig. 10c), suggesting that the estimated temperatures may not reflect deformation conditions. Instead, we argue that the heterogeneous textures between the coarse-grained and the fine-grained textures along the depth profile (Fig. 10a, b) could correspond to different degrees of deformation rather than differences in deformation conditions such as temperature (Fig. 11; e.g., Warren et al. 2008; Michibayashi et al. 2006, 2009).

7 Conclusions

Based on new geochemical and crystal-fabric data for peridotites of the 139°E Ridge (11°2′N, 139°3′E) in the westernmost side of Challenger Deep, we came to the following conclusions.

Peridotites consist of mantle harzburgite and dunite. Chemical compositions of spinel in the peridotites indicate a relatively fertile mantle with Cr# as low as 0.36. Furthermore, the elevated TiO_2 contents at medium values of Cr# (~0.5) of spinel and presence of interstitial plagioclase as well as the trace element compositions of pyroxene are characteristics closer to those of Parece Vela Rift peridotites rather than those of the Mariana forearc peridotites, suggesting that the Parece Vela Basin mantle could be exposed on the southwestern slope of the 139°E Ridge.

Peridotites have either coarse-grained texture (> 1 mm), heterogeneous intermediate texture, or fine-grained texture (< 0.5 mm). Coarse-grained peridotites are sampled from the shallowest part (3705–4042 m) of the dive area, whereas the fine-grained peridotites came from the deepest part (5996 m). Olivine crystal-fabrics vary with peridotite textures: two coarse-grained textures are associated with (010)[100] patterns, three fine-grained textures with {0kl}[100] patterns, and heterogeneous textures with various indistinct fabric patterns. The variations of the olivine textures and crystal-fabrics with depth suggest variations in the deformation process with depth. As a consequence, it is likely that a ductile shear zone could occur in the deepest part of the 139°E Ridge, by which the 139°E Ridge may have been uplifted at its base where the Caroline Ridge collided with the southern Mariana forearc.

Supplementary Information

The online version contains supplementary material available at https://doi.org/10.1186/s40645-022-00476-5.

Additional file 1. A collection of petrophysical and geochemical data for the 139°E Ridge peridotites shown in this study.

Acknowledgements

We acknowledge Prof. Bob Stern, two anonymous reviewers and Prof. M. Satish-Kumar for their constructive comments. We would like to thank the captain, crew, and scientists of the R/V *Yokosuka* and the *Shinkai6500* team for their assistance and professional work. OS and KM thank A/Prof. Hidemi Ishibashi of Shizuoka University for his fruitful advice and comments during this study. This work was supported by JSPS KAKENHI Grant Numbers 22244062, 26610160 and 16H06347.

Authors' contributions
KM and YO proposed the topic, conceived and designed the study. SO carried out the petrophysical and mineralogical study. FM and KN analyzed the bathymetric data and helped in their interpretation. FK and YL helped SO to analyze and interpret the geochemical data. SO, KM and YO prepared the manuscript and all authors reviewed and revised the text. All authors read and approved the final manuscript.

Funding
This work was supported by JSPS KAKENHI Grant Numbers 22244062, 26610160, and 16H06347.

Availability of data and materials
The datasets supporting the conclusions of this article are included within the article and its additional files.

Declarations

Competing interests
The authors declare that they have no competing interest.

Author details
[1]Department of Science, Graduate School of Integrated Science and Technology, Shizuoka University, Shizuoka 422-8529, Japan. [2]Department of Earth and Planetary Sciences, Graduate School of Environmental Studies, Nagoya University, Nagoya 464-8601, Japan. [3]Volcanoes and Earth's Interior Research Center, Research Institute for Marine Geodynamics, JAMSTEC, Yokosuka 237-0061, Japan. [4]Hydrographic and Oceanographic Department of Japan, Tokyo 100-8932, Japan. [5]Hawai'i Institute of Geophysics and Planetology, School of Ocean and Earth Science and Technology, University of Hawai'i at Mānoa, Honolulu, Hawai'i 96822, USA. [6]Institute of Earth Science, Academia Sinica, Taipei City 11529, Taiwan.

Received: 17 August 2021 Accepted: 14 March 2022
Published: 29 March 2022

References

Akizawa N, Ohara Y, Okino K, Ishizuka O, Yamashita H, Machida S, Sanfilippo A, Basch V, Snow JE, Sen A, Hirauchi K, Michibayashi K, Harigane Y, Fujii M, Asanuma H, Hirata T (2021) Geochemical characteristics of back-arc basin lower crust and upper mantle at final spreading stage of Shikoku Basin: an example of Mado Megamullion. Prog Earth Planet Sci 8:65. https://doi.org/10.1186/s40645-021-00454-3

Altis S (1999) Origin and tectonic evolution of the Caroline Ridge and the Sorol Trough, western tropical Pacific, from admittance and a tectonic modeling analysis. Tectonophysics 313:271–292. https://doi.org/10.1016/S0040-1951(99)00204-8

Anders E, Grevesse N (1989) Abundances of the elements: Meteroritic and solar. Geochim Cosmochim Acta 53:197–214. https://doi.org/10.1016/0016-7037(89)90286-X

Arai S (1994) Characterization of spinel peridotites by olivine-spinel compositional relationship: Review and interpretation. Chem Geol 59:279–293. https://doi.org/10.1016/0009-2541(94)90066-3

Armstrong AA (2010) U.S. Extended Continental Shelf Cruise to Map Sections of the Mariana Trench and the Eastern and Southern Insular Margins of Guam and the Northern Mariana Islands. UNH-CCOM/JHC Technical Report 1–45.

Avé Lallemant HG (1975) Mechanisms of preferred orientations in olivine in tectonite peridotites. Geology 3:653–656. https://doi.org/10.1130/0091-7613(1975)3%3C653:MOPOOO%3E2.0.CO;2

Ballhaus C, Berry RF, Green DH (1991) High pressure experimental calibration of the olivine-orthopyroxene-spinel oxygen geobarometer: implications for the oxidation state of the upper mantle. Contrib Mineral Petrol 107:27–40. https://doi.org/10.1007/BF00311183

Basch V, Sanfilippo A, Sani C, Ohara Y, Snow J, Ishizuka O, Harigane Y, Michibayashi K, Sen A, Akizawa N, Okino K, Fujii M, Yamashita H (2020) Crustal accretion in a slow spreading back-arc basin: insights from the Mado Megamullion oceanic core complex in the Shikoku Basin. Geohem Geophys Geosyst 21:e2020GC009199. https://doi.org/10.1029/2020GC009199

Beccaluva L, Maciotta G, Savelli C, Serri G, Zeda O (1980) Geochemistry and K–Ar ages of volcanics dredged in the Philippine Sea (Mariana, Yap, Palau trenches and Parece Vela Basin). In: Hayes DE (ed) The Tectonic and Geologic Evolution of Southeast Asian Seas and Islands, AGU Geophys Monogr Ser, **23**, pp 247–268.

Bloomer SH, Hawkins JW (1983) Gabbroic and ultramafic rocks from the Mariana Trench: An island arc ophiolite. In: Hayes DE (ed) AGU Geophys Monogr Ser, **27**, pp 294–317.

Blundy J, Wood B (1994) Prediction of crystal-melt partition coefficients from elastic moduli. Nature 372:452–454. https://doi.org/10.1038/372452a0

Bodinier JL, Godard M (2014) Orogenic, ophiolitic, and abyssal peridotites. In: Holland H, Turekian K (eds) Treatise on geochemistry (second edition), vol 3. Elsevier, pp 103–167

Bryndzia LT, Wood BJ (1990) Oxygen thermobarometry of abyssal spinel peridotites: the redox state and C-O-H volatile composition of the Earth's sub-oceanic upper mantle. Am J Sci 290:1093–1116. https://doi.org/10.2475/ajs.290.10.1093

Bunge HJ (1982) Texture analysis in materials sciences. Buttleworths, London, p 593

Cannat M, Mevel C, Maia M, Deplus C, Durand C, Gente P, Agrinier P, Belarouchi A, Dubuisson G, Humler E, Reynolds J (1995) Thin crust, ultramafic exposures, and rugged faulting patterns at the Mid-Atlantic Ridge (22°–24°N). Geology 23:49–52. https://doi.org/10.1130/0091-7613(1995)023%3C0049:TCUEAR%3E2.3.CO;2

Chen L, Tang L, Li X, Dong Y, Yu X, Ding W (2019) Geochemistry of peridotites from the Yap Trench, Western Pacific: implications for subduction zone mantle evolution. Int Geol Rev 61:1037–1051. https://doi.org/10.1080/00206814.2018.1484305

Dick HJB, Bullen T (1984) Chromian spinel as a petrogenetic indicator in abyssal and alpine-type peridotites and spatially associated lavas. Contrib Mineral Petrol 86:54–76. https://doi.org/10.1007/BF00373711

Dick HJB, Kvassnes AJS, Robinson PT, MacLeod CJ, Kinoshita H (2019) The Atlatis Bank gabbro massif, Southwest Indian Ridge. Prog Earth Planet Sci 6:64. https://doi.org/10.1186/s40645-019-0307-9

Escartín J, Smith D, Cann J, Schouten H, Langmuir CH, Escrig S (2008) Central role of detachment faults in accretion of slow-spreading oceanic lithosphere. Nature 455:790–794. https://doi.org/10.1038/nature07333

Fryer P, Becker N, Appelgate B, Martinez F, Edwards M, Fryer G (2003) Why is the challenger deep so deep? Earth Planet Sci Lett 211:259–269. https://doi.org/10.1016/S0012-821X(03)00202-4

Fujioka K, Okino K, Kanamatsu T, Ohara Y (2002) Morphology and origin of the challenger deep in the Southern Mariana Trench. Geophys Res Lett 29:1372. https://doi.org/10.1029/2001GL013595

Griffin WL, Powell WJ, Pearson NJ, O'Reilly SY (2008) GLITTER: Data reduction software for laser ablation ICP–MS. In: Sylvester P (ed) Laser Ablation ICP–MS in the Earth Sciences: Current practices and outstanding issues. Series 40. Mineralogical Association of Canada, Vancouver BC, pp 308–311.

Harigane Y, Michibayashi K, Ohara Y (2008) Shearing within lower crust during progressive retrogression: structural analyses of gabbroic rocks from the Godzilla Mullion, an oceanic core complex in the Parece Vela backarc basin. Tectonophysics 457:183–196. https://doi.org/10.1016/j.tecto.2008.06.009

Harigane Y, MichibayashiOhara K (2010) Amphibolitization within the lower crust in the termination area of the Godzilla Megamullion an oceanic core complex in the Parece Vela Basin. Isl Arc 19:718–730. https://doi.org/10.1111/j.1440-1738.2010.00741.x

Harigane Y, Michibayashi K, Ohara Y (2011a) Relicts of deformed lithospheric mantle within serpentinites and weathered peridotites from the Godzilla Megamullion, Parece Vela Back-arc Basin. Philippine Sea Isl Arc 20:174–187. https://doi.org/10.1111/j.1440-1738.2011.00759.x

Harigane Y, Michibayashi K, Ohara Y (2011b) Deformation and hydrothermal metamorphism of gabbroic rocks within the Godzilla Megamullion, Parece Vela Basin, Philippine Sea. Lithos 124:185–199. https://doi.org/10.1016/j.lithos.2011.02.001

Harigane Y, Okamoto A, Morishita T, Snow JE, Tamura A, Yamashita H, Michibayashi K, Ohara Y, Arai S (2019) Melt-fluid infiltration along detachment shear zones in oceanic complexes: insights from amphiboles in gabbro mylonites from the Godzilla Megamullion, Parece Vela Basin, the

Philippine Sea. Lithos 344–345:217–231. https://doi.org/10.1016/j.lithos.2019.06.019
Hart SR, Dunn T (1993) Experimental cpx/melt partitioning of 24 trace elements. Contrib Mineral Petrol 113:1–8. https://doi.org/10.1007/BF00320827
Hawkins J, Batiza R (1977) Metamorphic rocks of the Yap arc-trench system. Earth Planet Sci Lett 37:216–229. https://doi.org/10.1016/0012-821X(77)90166-2
Hellebrand E, Snow JE, Dick JB, Hofmann AW (2001) Coupled major and trace elements as indicators of the extent of melting in mid-ocean-ridge peridotites. Nature 410:677–681. https://doi.org/10.1038/35070546
Holtzman BK, Kohlstedt DL, Zimmerman ME, Heidelbach F, Hiraga T, Hustoft J (2003) Melt segregation and strain partitioning: implications for seismic anisotropy and mantle flow. Science 301:1227–1230. https://doi.org/10.1126/science.1087132
Ishii T, Robinson PT, Maekawa H, Fiske R (1992) Petrological studies of peridotites from diapiric serpentinite seamounts in the Izu-Ogasawara-Mariana forearc, Leg 125. Proc Ocean Drill Prog Sci Results 125:593–614
Ishizuka O, Tani K, Reagan MK, Kanayama K, Umino S, Harigane Y, Sakamoto I, Miyajima Y, Yuasa M, Dnkey DJ (2011) The timescales of subduction initiation and subsequent evolution of oceanic island arc. Earth Planet Sci Lett 306:229–240. https://doi.org/10.1016/j.epsl.2011.04.006
Ishizuka O, Yuasa M, Tamura Y, Shukuno H, Stern RJ, Naka J, Joshima M, Taylor RN (2010) Migrating shoshonitic magmatism tracks Izu–Bonin–Mariana intra-oceanic arc rift propagation. Earth Planet Sci Lett 294:111–122. https://doi.org/10.1016/j.epsl.2010.03.016
Jung H, Katayama I, Jiang Z, Hiraga T, Karato S (2006) Effect of water and stress on the lattice-preferred orientation of olivine. Tectonophysics 421:1–22. https://doi.org/10.1016/j.tecto.2006.02.011
Kakihata Y, Michibayashi K, Dick H (2022) Heterogeneity in texture and crystal-fabric of intensely hydrated ultramylonitic peridotites along a transform fault, Southwest Indian Ridge. Tectonophysics 829:229206. https://doi.org/10.1016/j.tecto.2021.229206
Kelemen PB, Dick HJB, Quick JE (1992) Formation of harzburgite by pervasive melt/rock reaction in the upper mantle. Nature 358:635–641. https://doi.org/10.1038/358635a0
Kohli A, Wolfson-Schwehr M, Prigent C, Warren JM (2021) Oceanic transform fault seismicity and slip mode influenced by seawater infiltration. Nat Geosci 14:606–611. https://doi.org/10.1038/s41561-021-00778-1
Le Roux V, Bodinier JL, Tommasi A, Alard O, Dautria JM, Vauchez A, Riches AJV (2007) The Lherz spinel lherzolite: refertilized rather than pristine mantle. Earth Planet Sci Lett 259:599–612. https://doi.org/10.1016/j.epsl.2007.05.026
Le Roux V, Tommasi A, Alard VA (2008) Feedback between melt percolation and deformation in an exhumed lithosphere–asthenosphere boundary. Earth Planet Sci Lett 274:401–413. https://doi.org/10.1016/j.epsl.2008.07.053
Loocke M, Snow JE, Ohara Y (2013) Melt stagnation in peridotites from the Godzilla Megamullion Oceanic Core Complex, Parece Vela Basin, Philippine Sea. Lithos 182–183:1–10. https://doi.org/10.1016/j.lithos.2013.09.005
MacLeod CJ, Searle RC, Murton BJ, Casey JF, Mallows C, Unsworth SC, Achenbach KL, Harris M (2009) Life cycle of oceanic core complexes. Earth Planet Sci Lett 287:333–344. https://doi.org/10.1016/j.epsl.2009.08.016
Mainprice D, Nicolas A (1989) Development of shape and lattice preferred orientations: application to the seismic anisotropy of the lower crust. J Struct Geol 11:175–189. https://doi.org/10.1016/0191-8141(89)90042-4
Mainprice D, Barruol G, Ismaïl WB (2000) The Seismic anisotropy of the Earth's mantle: from single crystal to polycrystal. In: Karato S, Forte AM, Liebermann RC, Masters G, Stixrude L (eds) Mineral Physics and Seismic Tomography: from Atomic to Global. Geophysical Monograph, American Geophysical Union, 117:237–264.
Mainprice D, Hielscher R, Schaeben H (2011) Calculating anisotropic physical properties from texture data using the MTEX open-source package. In: Prior DJ, Rutter EH, Tatham DJ (eds) Deformation Mechanisms, Rheology and Tectonics: Microstructures, Mechanics and Anisotropy, Geological Society, London, Special Publications, 360, 175–192.
McDonough WF, Sun SS (1995) The composition of the Earth. Chem Geol 120:223–253. https://doi.org/10.1016/0009-2541(94)00140-4
Michibayashi K, Harigane Y, Ohara Y, Muto J, Okamoto A (2014) Rheological properties of the detachment shear zone in an oceanic core complex inferred by plagioclase flow law: Godzilla Megamullion, Parece Vela back-arc basin, Philippine Sea. Earth Planet Sci Lett 408:16–23. https://doi.org/10.1016/j.epsl.2014.10.005
Michibayashi K, Ina T, Kanagawa K (2006) The effect of dynamic recrystallization on olivine fabric and seismic anisotropy: Insight from a ductile shear zone, Oman ophiolite. Earth Planet Sci Lett 244:695–708. https://doi.org/10.1016/j.epsl.2006.02.019
Michibayashi K, Mainprice D (2004) The role of pre-existing mechanical anisotropy on shear zone development within Oceanic Mantle Lithosphere: an example from the Oman Ophiolite. J Petrol 45:405–414. https://doi.org/10.1093/petrology/egg099
Michibayashi K, Tasaka M, Ohara Y, Ishii T, Okamoto A, Fryer P (2007) Variable microstructure of peridotite samples from the southern Mariana Trench: evidence of a complex tectonic evolution. Tectonophysics 444:111–118. https://doi.org/10.1016/j.tecto.2007.08.010
Michibayashi K, Tominaga M, Ildefonse B, Teagle DAH (2019) What lies beneath: the formation and evolution of oceanic lithosphere. Oceanography 32:138–149. https://doi.org/10.5670/oceanog.2019.136
Michibayashi K, Ohara Y, Stern RJ, Fryer P, Kimura JI, Tasaka M, Ishii T (2009) Peridotites from a ductile shear zone within back-arc lithospheric mantle, southern Mariana Trench: Results of a Shinkai 6500 dive. Geochem Geophys Geosys 10:1–17. https://doi.org/10.1029/2008GC002197
Michibayashi K, Mainprice D, Fujii A, Uehara S, Shinkai Y, Kondo Y, Ohara Y, Ishii T, Fryer P, Bloomer SH, Ishiwatari A, Hawkins JW, Ji S (2016a) Natural olivine crystal-fabrics in the western Pacific convergence region: a new method to identify fabric type. Earth Planet Sci Lett 443:70–80. https://doi.org/10.1016/j.epsl.2016.03.019
Michibayashi K, Watanabe T, Harigane Y, Ohara Y (2016b) The effect of a hydrous phase on seismic anisotropy in the oceanic lower crust: a case study from the Godzilla Megamullion, Philippine Sea. Isl Arc 25:209–219. https://doi.org/10.1111/iar.12132
Miller MS, Kennett BLN, Toy VG (2006) Spatial and temporal evolution of the subducting Pacific plate structure along the western Pacific margin. J Geophys Res 111:1–14. https://doi.org/10.1029/2005JB003705
Nicolas A, Boudier F, Boullier AM (1973) Mechanism of flow in naturally and experimentally deformed peridotites. Amer J Sci 273:853–876. https://doi.org/10.2475/ajs.273.10.853
Nicolas A, Poirier JP (1976) Crystalline plasticity and solid state flow in metamorphic rocks. John Wiley, London, p 444
Nicolas A (1989) Structure of Ophiolites and Dynamics of Oceanic Lithosphere. Kluwer Academic Publishers, London, p 380
Ohara Y (2003) Reviews on mantle peridotites from the Philippine Sea back-arc spreading systems. Rep Hydrogr Oceanogr Res 39:63–83
Ohara Y (2016) The Godzilla megamullion, the largest oceanic core complex on the earth: a historical review. Isl Arc 25:193–208. https://doi.org/10.1111/iar.12116
Ohara Y, Fujioka K, Ishii T, Yurimoto H (2003) Peridotites and gabbros from the Parece Vela backarc basin: unique tectonic window in an extinct backarc spreading ridge. Geochem Geophys Geosyst 4:8611. https://doi.org/10.1029/2002GC000469
Ohara Y, Fujioka K, Ishizuka O, Ishii T (2002a) Peridotites and volcanics from the Yap arc system: implications for tectonics from the Yap arc system: implications for tectonics of the southern Philippine Sea Plate. Chem Geol 189:35–53. https://doi.org/10.1016/S0009-2541(02)00062-1
Ohara Y, Ishii T (1998) Peridotite from the southern Mariana forearc: heterogeneous fluid supply in mantle wedge. Isl Arc 7:541–558. https://doi.org/10.1111/j.1440-1738.1998.00209.x
Ohara Y, Martinez F, Brounce MN, Pujana I, Ishii T, Stern RJ, Ribeiro J, Michibayashi K, Kelly KA, Reagan MK, Watanabe H, Okumura T, Oya S, Mizuno T (2014) The first Shinkai dive study of the southwestern Mariana arc system. AGU Fall Meeting 2014: T53A4651.
Ohara Y, Stern RJ, Ishii T, Yurimoto H, Yamazaki T (2002b) Peridotites from the Mariana Trough: first look at the mantle beneath an active back-arc basin. Contrib Mineral Petrol 143:1–18. https://doi.org/10.1007/s00410-001-0329-2
Ohara Y, Yoshida T, Kato Y, Kasuga S (2001) Giant Megamullion in the Parece Vela Backarc Basin. Mar Geophys Res 22:47–61. https://doi.org/10.1023/A:1004818225642
Okino K, Kasuga S, Ohara Y (1998) A new scenario of the Parece Vela Basin genesis. Mar Geophys Res 20:21–40. https://doi.org/10.1023/A:1004377422118

Parkinson IJ, Arculus RJ (1999) The redox state of subduction zones: insights from arc-peridotites. Chem Geol 160:409–423. https://doi.org/10.1016/S0009-2541(99)00110-2
Piccardo GB, Zanetti A, Muntener O (2007) Melt/peridotite interaction in the Southern Lanzo peridotite: field, textural and geochemical evidence. Lithos 94:181–209. https://doi.org/10.1016/j.lithos.2006.07.002
Rampone E, Piccardo GB, Vannucci R, Bottazzi P (1997) Chemistry and origin of trapped melts in ophiolitic peridotites. Geochim Cosmochim Acta 61:4557–4569. https://doi.org/10.1016/S0016-7037(97)00260-3
Rampone E, Piccardo GB, Hofmann AW (2008) Multi-stage melt–rock interaction in the Mt. Maggiore (Corsica, France) ophiolitic peridotites: microstructural and geochemical evidence. Contrib Mineral Petrol 156:453–475. https://doi.org/10.1007/s00410-008-0296-y
Reagan MK, Heywood L, Goff K, Michibayashi K, Foster T Jr, Jicha B, Lapen T, McClelland WC, Ohara Y, Righter M, Scott S, Sims KWW (2018) Geodynamic implications of crustal lithologies from the southeast Mariana forearc. Geosphere. https://doi.org/10.1130/GES01536.1
Reagan MK, Ishizuka O, Stern RJ, Kelley KA, Ohara Y, Blichert-Toft J, Bloomer SH, Cash J, Fryer P, Hanan BB, Hickey-Vargas R, Ishii T, Kimura J, Peate DW, Rowe MC, Woods M (2010) Fore-arc basalts and subduction initiation in the Izu-Bonin-Mariana system. Geochem Geophys Geosyst. https://doi.org/10.1029/2009GC002871
Reagan MK, McClelland WC, Girard G, Goff KR, Peate DW, Ohara Y, Stern RJ (2013) The geology of the southern Mariana fore-arc crust: Implications for the scale of Eocene volcanism in the western Pacific. Earth Planet Sci Lett 380:41–51. https://doi.org/10.1016/j.epsl.2013.08.013
Ribeiro J, Stern RJ, Martinez F, Ishizuka O, Merle SG, Kelley K, Anthony EY, Ren M, Ohara Y, Reagan M, Girard G, Bloomer S (2013a) Geodynamic evolution of a forearc rift in the southernmost Mariana arc. Isl Arc 22:453–476. https://doi.org/10.1111/iar.12039
Ribeiro J, Stern RJ, Kelly KA, Martinez F, Ishizuka O, Manton WI, Ohara Y (2013b) Nature and distribution of slab-derived fluids and mantle sources beneath the Southeast Mariana forearc rift. Geochm Geophys Geosyst 14:4585–4607. https://doi.org/10.1002/ggge.20244
Sato M (1978) Oxygen fugacity of basaltic magmas and the role of gasforming elements. Geophys Res Lett 5:447–449. https://doi.org/10.1029/GL005I006P00447
Sato H, Ishii T (2011) Petrology and mineralogy of mantle peridotites from the southern Marianas. In: Ogawa Y, Anma R, Dilek Y (eds) Accretionary Prisms and Convergent Margin Tectonics in the Northwest Pacific Basin. Springer Nature, Switzerland, Modern Approaches in Solid Earth Sciences 8:129–148.
Seyler M, Toplis MJ, Lorand JP, Luguet A, Cannat M (2001) Clinopyroxene microtextures reveal incompletely extracted melts in abyssal peridotites. Geology 29:155–158. https://doi.org/10.1130/0091-7613(2001)029%3C0155:CMRIEM%3E2.0.CO;2
Skemer P, Katayama I, Jiang Z, Karato S (2005) The misorientation index: development of a new method for calculating the strength of lattice-preferred orientation. Tectonophysics 411:157–167. https://doi.org/10.1016/j.tecto no.2005.08.023
Sleeper JD, Marinez F, Fryer P, Stern RJ, Kelley KA, Ohara Y (2021) Diffuse spreading, a newly recognized mode of crustal accretion in the southern Mariana Trough backarc basin. Geosphere. https://doi.org/10.1130/GES02360.1
Stern RJ (2010) The anatomy and ontogeny of modern intra-oceanic arc systems. In: Kusky TM, Zhai MG, Xiao W (eds) The Evolving Continents: Understanding Processes of Continental Growth. Geological Society, London, Special Publications, 338:7–34.
Stern RJ, Ohara Y, Ren M, Leybourne M, Bowers B (2020) Glimpses of oceanic lithosphere of the challenger deep Forearc segment in the Southernmost Marianas: The 143°E Transect, 5800–4200 m. Isl Arc 29:e12359. https://doi.org/10.1111/iar.12359
Tani K, Dunkley DJ, Ohara Y (2011) Termination of backarc spreading: zircon dating of a giant oceanic core complex. Geology 39:47–50. https://doi.org/10.1130/G31322.1
Tommasi A, Mainprice D, Canova G, Chastel Y (2000) Viscoplastic self-consistent and equilibrium-based modeling of olivine lattice preferred orientations: implications for the upper mantle seismic anisotropy. J Geophys Res 105:7893. https://doi.org/10.1029/1999JB900411
Tommasi A, Tikoff B, Vauchez A (1999) Upper mantle tectonics: three-dimensional deformation, olivine crystallographic fabrics and seismic properties. Earth Planet Sci Lett 168:173–186. https://doi.org/10.1016/S0012-821X(99)00046-1
Tommasi A, Vauchez A, Ionov DA (2008) Deformation, static recrystallization, and reactive melt transport in shallow subcontinental mantle xenoliths (Tok Cenozoic volcanic field, SE Siberia). Earth Planet Sci Lett 272:65–77. https://doi.org/10.1016/j.epsl.2008.04.020
Tucholke BE, Lin J, Kleinrock MC (1998) Megamullions and mullion structure defining oceanic metamorphic core complexes on the Mid-Atlantic Ridge. J Geophys Res Solid Earth 103:9857–9866. https://doi.org/10.1029/98JB00167
Yanagida Y, Ishiwatari A, Ishii T (2007) Forearc-backarc mantle exposed on the landward slope of the southern Mariana Trench: a result of the Hakuho-Maru KH03-3 cruise. Chikyu Monthly 29:615–627
Warren JM, Hirth G, Kelemen PB (2008) Evolution of olivine lattice preferred orientation during simple shear in the mantle. Earth Planet Sci Lett 272:501–512. https://doi.org/10.1016/j.epslo.2008.03.063
Wheeler J, Prior DJ, Jiang Z, Spiess R, Trimby PW (2001) The petrological significance of misorientations between grains. Contrib Mineral Petrol 141:109–124. https://doi.org/10.1007/s004100000225
Zhang S, Karato S (1995) Lattice preferred orientation of olivine aggregates deformed in simple shear. Nature 375:774–777. https://doi.org/10.1038/375774a0
Zhou H, Dick HJB (2013) Thin crust as evidence for depleted mantle supporting the Marion Rise. Nature 494:195–200. https://doi.org/10.1038/nature11842

Publisher's Note